ORIGINAL PAPER

Enhanced Magnetic and Optoelectronic Properties of Cu-Doped ZnO: Mn Nanoparticles Synthesized by Solution Combustion Technique

B. Yasoda[1] · K. Sunil Kumar[2] · M. Ramanadha[2] · A. Sudharani[2] · R. P. Vijayalakshmi[2] 📵

Abstract

Nano-ZnO and ZnO doped with Cu: Mn samples (Mn = 2% and Cu = 2% and 4%) have been synthesized by combustion synthesis. The effect of Cu content (Cu/Mn co-dopant) on the structural, optical, and magnetic properties has been studied. X-ray diffraction studies revealed hexagonal Wurtzite structure, and the particle size is around 36–18 nm. From scanning electron microscopy (SEM) analysis, morphology of all the samples was spherical in shape with high porous structure. The elemental composition of the synthesized samples was investigated using energy dispersive X-ray analysis (EDAX), which confirmed the presence of selective elements in the samples near stoichiometric ratio. FTIR spectra confirmed the presence of functional groups in synthesized samples. From UV–Vis absorbance spectra, blue shift is observed with increasing dopant concentration. From VSM studies, the enhanced magnetization properties were observed in doped samples. From photoluminescence (PL) studies, decrease in rate of recombination of electron–hole pairs is observed. The simultaneous enrichment of magnetic and optical properties of Cu doped ZnO: Mn nanoparticles can be used in future spintronic and optoelectronic devices.

1 Introduction

During the last three decades, dilute magnetic semiconductors (DMS) have attracted great interest because of tuning magnetic behavior, by doping with magnetic element in nonmagnetic semiconductor. Therefore, there is an opportunity in DMS to use degrees of freedom of load and rotation for various applications, especially if the DMS can be made ferromagnetic. In fact, the term "spintronics" is becoming increasingly popular when describing devices that will use the spin and charge of electrons in these semiconductor materials [1–3]. Zinc oxide (ZnO) has a Wurtzite hexagonal phase with a wide band gap (~3.3 eV). It is an unecological compound and has a piezoelectric effect [4]. Because of its significant physical and chemical properties, ZnO appears to be an extremely important host material for many applications in many technologies, such as optoelectronic devices, nanosensors, nanogenerators, electronics, spintronics, and photocatalysts [5–9]. The performance of the ZnO nanoparticles can be improved by controlling the dopant and dopant concentrations. The unique feature of DMS is that the doping of transition material (TM) into a semiconductor does not affect the crystal structure but tentatively modifies its magnetic, dielectric, and optical properties [10, 11].

Lot of research is carried out on transition metal (TM), rare earth (RE), and alkaline earth (AE) metal ions doped ZnO-based DMS. It should be noted that Mn-doped ZnO has been synthesized to study its possible applications in spintronic devices by effectively utilizing its unique electrical, magnetic, and luminescent properties [12–14]. Theoretical studies have shown the presence of ferromagnetism in manganese-doped ZnO nanomaterials. Several methods are available to prepare doped and pure ZnO nanopowders, such as hydrothermal [15], chemical cationic surfactant assisted [16], microwave-assisted combustion [17, 18], co-precipitation [19], sol-gel [20], and combustion [21, 22]. In the case of large-scale economic production of nanostructured DMS, combustion methods are the most efficient. It has an acceleration rate, a versatility of the reaction conditions applied, a lower consumption of time, and a higher chemical yield and synthesis. The transition is faster and more profitable [23].

✉ R. P. Vijayalakshmi
vijayaraguru@gmail.com

1 Department of Physics, D R W College, 524101, Gudur, India

2 Department of Physics, Sri Venkateswara University, 517502, Tirupati, India

Solution combustion technique is a promising alternative synthesis method due to its simple preparation, its suitability for any type of doping, and its very easy control of particle size. The combustion process has several advantages over other growth processes, such as the use of simple equipment, growth without catalysts, and low cost [23]. This method has also been used successfully to prepare nanoscale ZnO and other luminescent materials.

Muniraja et al. [24] reported that ZnO nanoparticles synthesized at 500 °C is the best one for memory devices in spintronics applications. Janardhan et al. [25] reported the decrease of optical band gap and particle size with increasing of Ni concentration. Umadevi et al. [26] reported the decrease of optical band gap and particle size with increasing of Co concentration. Irshad et al. [27] also reported the decrease of optical band gap and enhancement of magnetization properties in Fe-/Cr-doped ZnO nanoparticles. Amarjyothi et al. [28] reported that low-doping concentration of Mn in ZnO nanoparticles enhances the magnetization and reduction in optical band gap properties. Othmon et al. [29] reported the quenching of PL intensity and ferromagnetism at room temperature in Mn-doped ZnO nanoparticles.

Moreover, ounce of literature were available on the solution combustion synthesis of pure ZnO and different metal ions (TM, RE, and AE) doped nanoparticles. No reports are available on Cu-doped ZnO: Mn nanoparticles synthesized in solution combustion method, and scope of present work is to improve magnetization and photoluminescence studies. In the present paper, we discussed the XRD, SEM, EDAX, FTIR, and UV–Vis. Absorbance, VSM, and PL studies on Cu doped ZnO: Mn nanoparticles.

2 Experimental and Characterization Studies

2.1 Materials

Zinc nitrate ($Zn(NO_3)_2.6H_2O$), copper nitrate ($Cu(NO_3)_2.2.5H_2O$), manganese acetate ($Mn(CH_3COO)_2.4H_2O$, urea ($CO(NH_2)_2$, polyethylene glycol (PEG-400), and ammonium solution (NH_3) were used as starting materials. All the chemicals were purchased from Sigma–Aldrich and HiMedia and were used without further purifications.

2.2 Method

Zinc nitrate and urea were dissolved each in 40 ml of deionized water separately with 1:5 molar ratio and stirred for 30 min. After that, urea solution was added dropwise to zinc nitrate solution and stirred for 30 min, and then NH_3 solution is added dropwise to the above mixed solution until the pH reaches to 9; the solution becomes white, and then

continuously stirred for 10 min. After that, 2 ml of PEG solution was added to above solution and stirring was continued for 7 h. Finally the solution was kept in a closed muffle furnace at 500 °C combustion temperature for 1 h [24]. To synthesize ZnO: Mn (2%) and Cu-doped ZnO: Mn (2% and 4%) samples, similar process followed. All the synthesized samples were annealed at 600 °C for 1 h. The samples were named pure ZnO as (ZnO), ZnO: Mn (2%) as (ZMCO-0), and Cu-doped ZnO: Mn (2% and 4%) as (ZMCO-2 and ZMCO-4)

2.3 Characterization Techniques

The synthesized samples were subjected to various characterizations. The crystal structure of synthesized samples was determined by X-ray diffractometer (XRD) with Cu-Kα radiation (λ = 0.154 nm). Surface morphology, compositional analysis, and particle size were analyzed by scanning electron microscope (SEM) attached with energy dispersive analysis of X-ray spectra (EDAX) (ZEISS EVO MA-15). Fourier transform infrared spectroscopy (FTIR) was recorded with a Thermo Nicolet 6700 spectrophotometer, and optical properties were characterized by using UV–Vis absorption spectrometer (Varian: 5000). The magnetization hysteresis (M-H) loops were evaluated at room temperature using a vibrating sample magnetometer (VSM) (Lakeshore: 7410). Photoluminescence (PL) emission properties were carried out with fluoro emission spectrometer (FLUOROLOG-FL3-11) using Xe lamp (400 Watt) at 425 nm excitation wavelength.

3 Results and Discussions

3.1 Structural Analysis

Figure 1 shows the XRD studies of ZnO, ZMCO-0, ZMCO-2, and ZMCO-4 nanoparticles prepared by solution combustion method at different concentrations. All XRD peaks of ZnO nanoparticles correspond to the hexagonal phase with Wurtzite structure. It has been observed that the nine reflection peaks of 2θ with the corresponding values of the Miller indices (hkl) are 31.8° (100), 34.35° (002), 36.22° (101), 47.59° (102), 56.51° (110), 62.89° (103), 66.69° (200), and 69.09° (201); these are perfectly matched with JCPDS Card No. 05-0664, and there is no indication of secondary phase [30]. From XRD spectra, it can be observed that there is a clear shift towards the higher angle side at the position of 2θ around 36° in ZMCO-0, ZMCO-2, and ZMCO-4 in doped nanoparticles. This shift indicates that the lower ionic radii of Cu and Mn were incorporated in to the Zn site of ZnO material. This type of shift is also observed in FTIR and UV–Vis absorption studies.

Fig. 1 (a) XRD spectra of ZnO- and Cu-doped ZnO: Mn nanoparticles and (b) enlarged view of XRD spectra at 36°
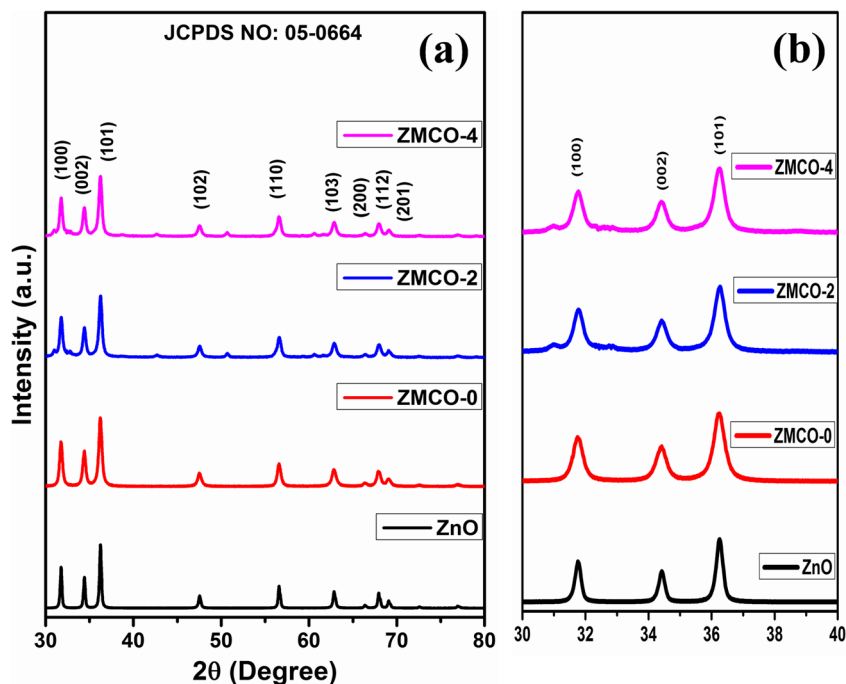
Broadening of the XRD peak to half of the maximum intensity indicates full width at half maximum (FWHM); it was used to calculate the average size of the crystallites of the nanoparticles. The broad peaks indicate the decrease in crystallinity. Crystallite sizes of ZnO nanoparticles were calculated from FWHM of most intense peak using the Debye–Scherrer formula [31],

$$\text{Crystallite size (D)} = \frac{0.9\,\lambda}{\beta\,Cos\theta}$$

where λ is the wavelength of Cu-Kα radiation, β is FWHM of maxima peak, and θ is the diffraction angle; it is presented in Table 1.

From the Table 1, we noticed that the crystallite size is decreased in doped samples compared to ZnO samples. As Cu concentration increases in ZnO: Mn nanoparticles, FWHM increases. It is due to decrease of lattice contraction and increase of micro-strain because of smaller ionic radius of Cu and Mn than Zn. The size of nanoparticles is around 36–18 nm.

Table 1 Structural parameters information of ZnO- and Cu-doped ZnO: Mn nanoparticles from XRD spectra

S.No.	Sample	a = b (Å)	c (Å)	D (nm)	c/a	V (Å)³
1	ZnO	3.254	5.214	36.12	1.60	47.82
2	ZMCO-0	3.240	5.204	26.71	1.60	47.30
3	ZNCO-2	3.238	5.201	21.32	1.60	47.21
4	ZMCO-4	3.233	5.198	18.56	1.60	47.05

### 3.2 Morphology and Compositional Analysis

The SEM images in Fig. 2(a–d) show morphology of ZnO, ZMCO-0, ZMCO-2, and ZMCO-4 nanoparticles synthesized by solution combustion method. The morphological change in the shape and size of the particles is remarkable. The appearance of the morphological change in shape and particle size can be attributed to the incorporation of Mn^{2+} and Cu^{2+} into Zn^{2+} sites during crystallization. As doping concentration of Cu increases in Zn site of ZnO: Mn, morphology of all the samples is spherical with smaller size and more homogeneous size distribution.

The chemical compositions of the synthesized samples were analyzed by energy-dispersive analysis of X-ray spectroscopy (EDAX) and the corresponding spectrum. Figure 3(a–d) shows the EDAX spectrum of ZnO, ZMCO-0, ZMCO-2, and ZMCO-4 samples which were recorded with SEM attached EDAX spectrometer. All the selective elements of Zn, Mn, Cu, and O were presented in near stoichiometric ratio in synthesized samples with free of impurities, and the compositions were noted in Table 2.

3.3 FTIR Analysis

The functional groups were observed by the Fourier transform infrared spectroscopy (FTIR) recorded at room temperature in the range of 400–4000 cm^{1}. Figure 4 shows the FTIR spectra of ZnO, ZMCO-0, ZMCO-2, and ZMCO-4 nanoparticles synthesized by solution

**Fig. 2** (a–d) SEM micrographs of ZnO- and Cu-doped ZnO: Mn nanoparticles
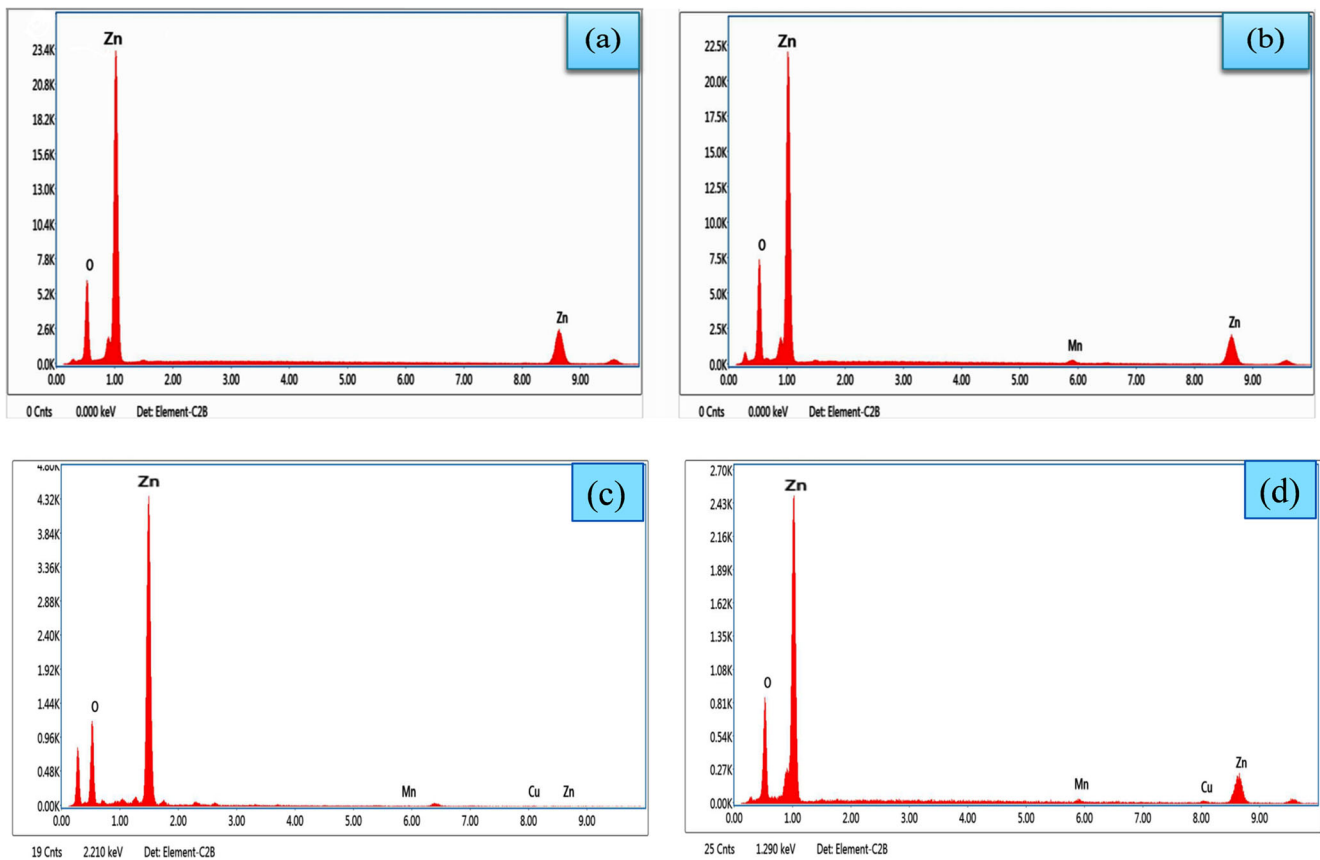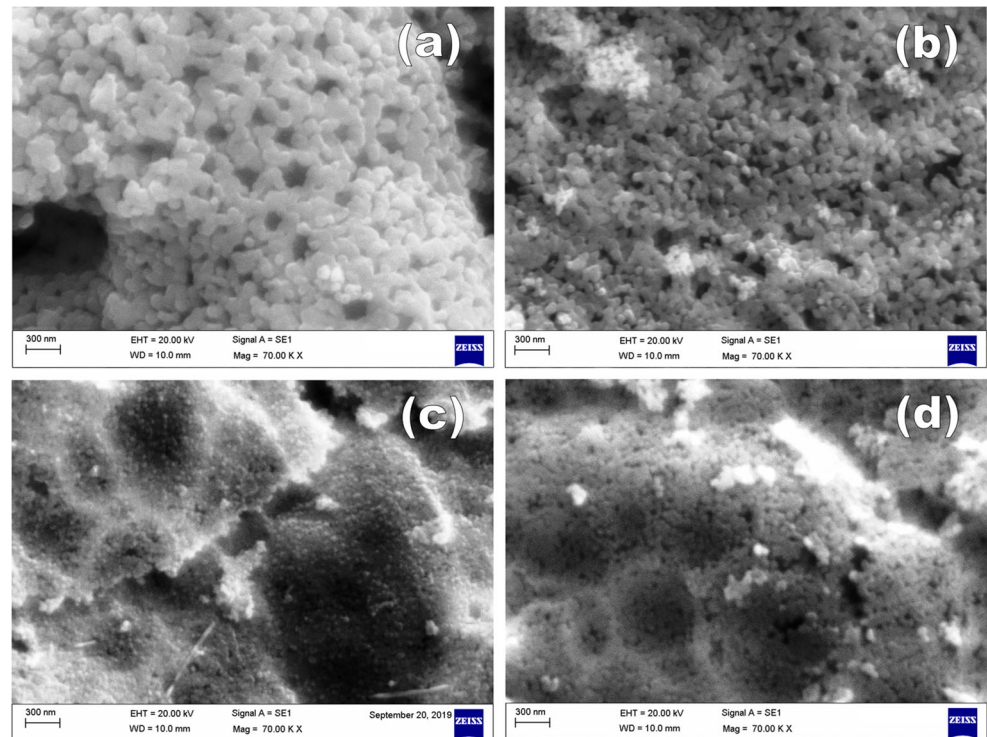
Fig. 3 (a–d) EDAX spectra of ZnO- and Cu-doped ZnO: Mn nanoparticles

Table 2 Compositional information of ZnO- and Cu-doped ZnO: Mn nanoparticles from EDAX spectra

S.No.	Sample	Elemental compositions (at %)				Total
		Zn	Mn	Cu	O	
1	ZnO	79.67	—	—	20.33	100
2	ZMCO-0	77.47	2.12	—	20.41	100
3	ZNCO-2	75.80	2.3	2.4	19.5	100
4	ZMCO-4	73.26	2.2	4.2	19.34	100

combustion method. The absorption band at around 450 cm^{-1} corresponds to the metal-oxy functional group presented in synthesized samples (Zn-O). The absorption band at around 1380 cm^{-1} corresponds to the symmetrical stretching mode of the carboxylate ion (stretching vibration mode of C-O) [32, 33]. The bond observed at around 1650 cm^{-1} denotes the reactive carbon during the synthesis process time. The bond at 2940 cm^{-1} corresponds to the vibration peak of stretching C-H bond. The fundamental mode of broad absorption band at 3420 cm^{-1} corresponds to the vibration and deformation of the O-H stretching bond, attributed to the water absorption on the metal surface [33]. All the functional groups were attributed to synthesized samples. From the graph, it is observed that the absorption band at around 450 cm^{-1} is slightly shifting towards the higher wavenumber side, which indicates the incorporation of Mn and Cu ions into Zn site ZnO material. This type of shift indicates the decrease of crystalline size, lattice parameters, and optical band gap values. These results were correlated with XRD and UV–Vis absorption studies.
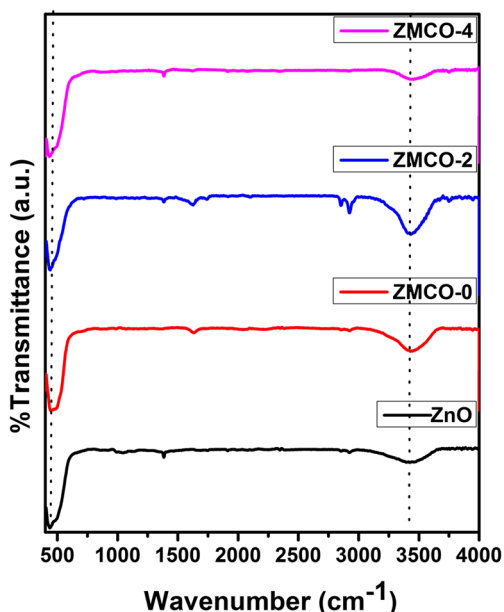
Fig. 4 FTIR spectra of ZnO- and Cu-doped ZnO: Mn nanoparticles
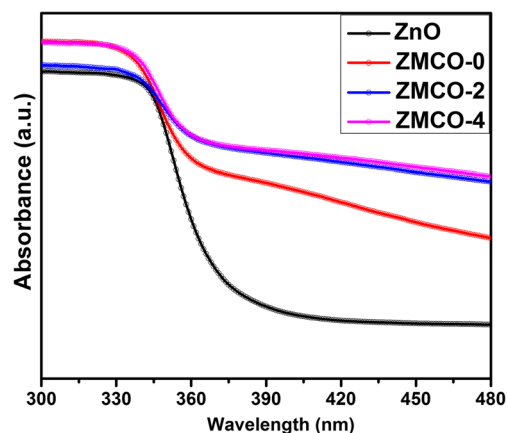
Fig. 5 UV–Vis absorbance spectra of ZnO- and Cu-doped ZnO: Mn nanoparticles

### 3.4 Optical Absorbance Studies

Optical absorption studies were performed by using UV–Vis. absorbance spectrometer. Figure 5 shows optical absorption spectra of ZnO nanoparticles. From the spectra, it is noticed that the absorption edge of doped samples (ZMCO-0, ZMCO-2, and ZMCO-4) were shifted towards higher wavelengths compared to ZnO sample. This alter towards the higher wavelength of light energy involves a decrease in band gap of the doped samples as confirmed by analysis of spectroscopic data using Tauc's plot graphs. From the UV–Vis. absorbance results, Tauc's plots are drawn by using the Tauc's relation [34],

$$(\alpha h\nu)^2 = C'(h\nu - Eg)$$

where α is the optical absorption coefficient of the material, h is the Planck constant, λ is the wavelength, C' is the proportionality constant, ν is the light frequency, and Eg is the band gap energy. From $(\alpha h\nu)^2$ versus $h\nu$ plot by extrapolating the linear part of the graph to the X-axis, the intersection value on X-axis will give the band gap.

The Tauc plots for the ZnO, ZMCO-0, ZMCO-2, and ZMCO-4 samples synthesized by the solution combustion method were shown in Fig. 6, respectively. The band separation values obtained from the graphs are listed in Table 3. The band gap energies for the ZnO, ZMCO-0, ZMCO-2, and ZMCO-4 samples are 3.32, 3.31, 3.13, and 3.04 eV, respectively. The ZMCO-4 sample has the lowest band gap with respect to ZnO and ZMCO-0, due to the influence of the Cu content. It is observed that for all sample groups, the band gap energy of nanomaterials is greater than their micron-sized materials. Enlargement of the forbidden band of nanomaterials is attributed to the quantum mechanical effects of small crystallites. In these length scales, the superimposed energy levels extend to be more quantified, producing a band gap that widens in the materials [35, 36]. It is also observed that the doped materials have the opposite behavior, namely, a forbidden narrowing of the strips with respect to the ZnO samples.

Fig. 6 Tauc's plots of ZnO- and Cu-doped ZnO: Mn nanoparticles
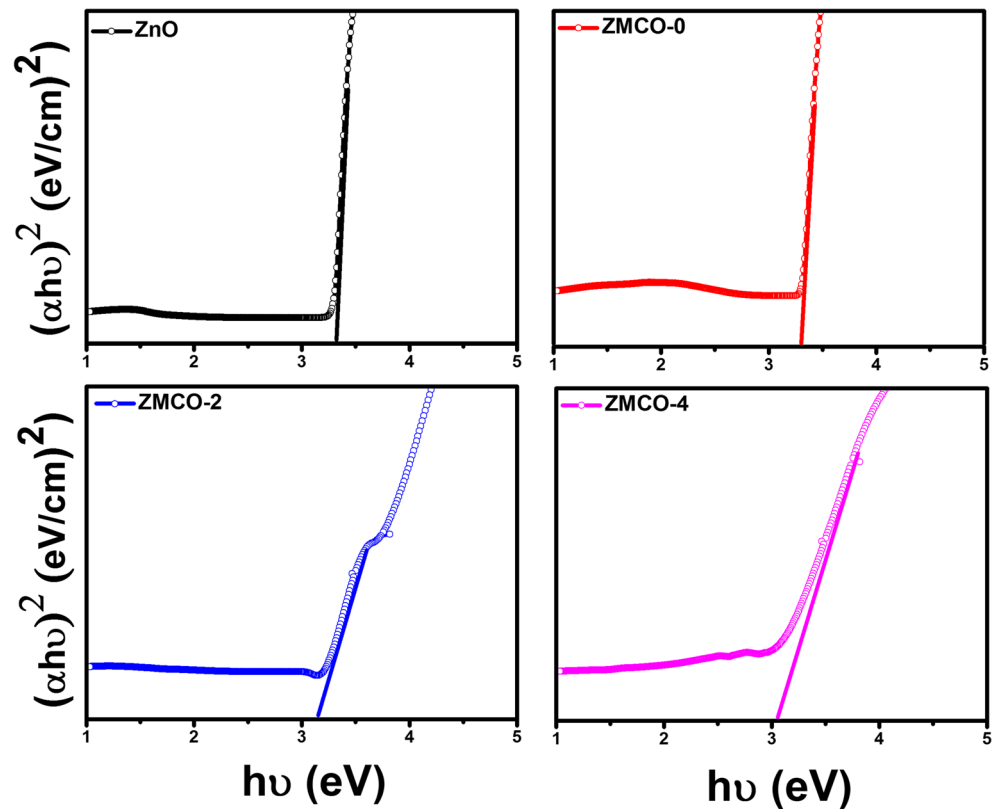
The forbidden band energies of the doped samples (ZMCO-0, ZMCO-2, and ZMCO-4) are less than ZnO, and this is true in all cases if the crystallites are of in nanosize. This is attributed to the presence of a mixture of Cu^{2+} and Mn^{2+} in the lattice of doped samples because Cu and Mn can coexist in their oxidation states.

3.5 Magnetization Studies

M-H hysteresis loop of synthesized samples was recorded by using vibrating sample magnetometer (VSM) at room temperature. Figure 7 shows the M-H hysteresis loop of ZnO, ZMCO-0, ZMCO-2, and ZMCO-4 recorded at room temperature. In ZnO sample, ferromagnetism should be strongly influenced by size, shape, and the surface to volume ratio of nanoparticles. Nanoparticles with high surface-to-volume ratio may have ferromagnetic-related defects [20]. From the

Table 3 Optical band gap information of ZnO- and Cu-doped ZnO: Mn nanoparticles from Tauc's plots

S.No.	Sample	Eg (eV)
1	ZnO	3.32
2	ZMCO-0	3.31
3	ZNCO-2	3.13
4	ZMCO-4	3.04

figure, it is observed that all the samples exhibited ferromagnetic nature of exchange interactions; magnetization parameters (saturation magnetization and remanent magnetization) also increase with increasing the doping concentration compared to ZnO sample and were noted in Table 4. However, various models like bound magnetic polaron (BMP), superexchange, Ruderman–Kittel–Kasuya–Yosida (RKKY), and double exchange have been proposed to understand the evolution of magnetic property in ZnO nanomaterials [37].

Since Cu and Mn doping in ZnO nanoparticles is desperately diluted, the need for direct interaction between magnetic ions is not possible for the double-exchange mechanism. In addition, since ZnO is a semiconductor, low doping of the Cu and Mn ions cannot renew it in the structural deformations. The free electron model based on RKKY is therefore unacceptable. As indicated in the PL spectrum, the Cu- and Mn-doped ZnO nanoparticles consist of vacant zinc defects and oxygen-related defects. In addition, an intrinsic exchange interaction due to individually ionized oxygen promotes BMPs and enhances ferromagnetic properties at room temperature. Therefore, we adopt the BMP mechanism to corroborate the evolution of magnetic property in ZnO nanoparticles [38].

Therefore, it is expected that the improvement in ferromagnetism for the Cu-/Mn-associated ZnO sample at room temperature is caused by the increase in the concentration of coupling oxygen vacancies and Cu/Mn ions, whereas the exchange interaction of Cu^{2+} and Mn^{2+} ions with the electrons

Fig. 7 M-H hysteresis curves of ZnO- and Cu-doped ZnO: Mn nanoparticles
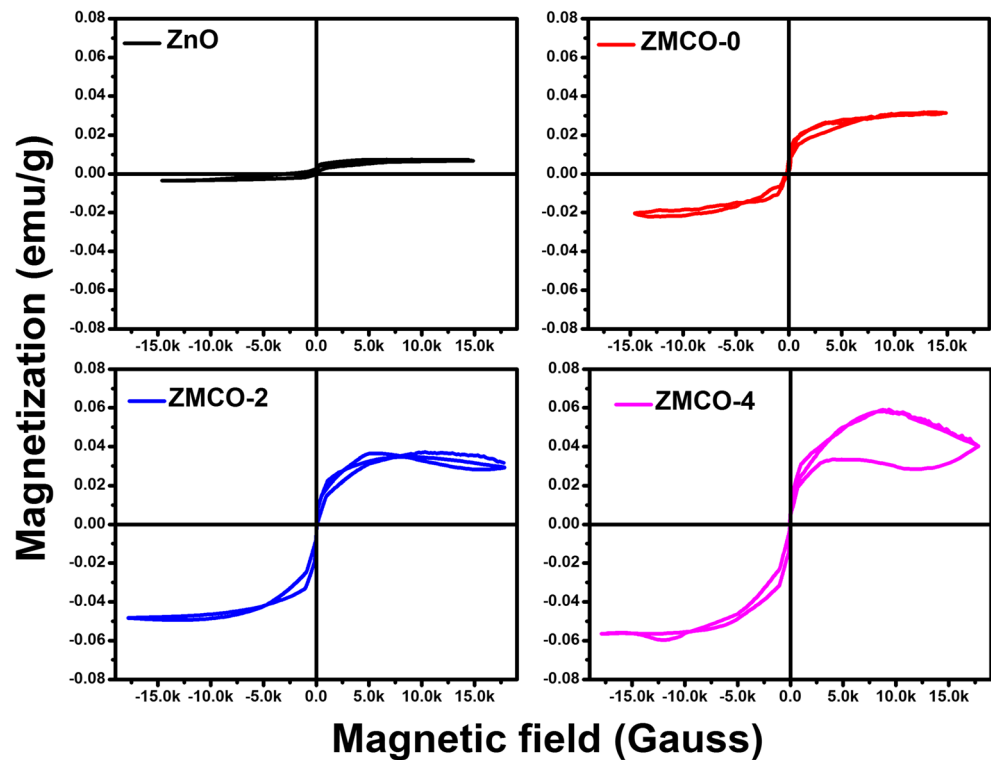
trapped in the oxygen vacancies will align the spins of the two dopant ions in a parallel configuration. The exchange interaction between the F-center and the BMP model was used to explain the ferromagnetism in these samples. Where, the electrons trapped in the oxygen vacancies can couple with Cu^{2+} ions or Mn^{2+} and induce a long-range ferromagnetic order in the synthesized samples [39]. The presence of Cu/Mn or Mn will increase oxygen deficiency and magnetic ion concentrations, and both factors will increase the number of overlays improving ferromagnetism. The results obtained suggest the use of Cu/Mn dopants to effectively improve the magnetic properties of ZnO.
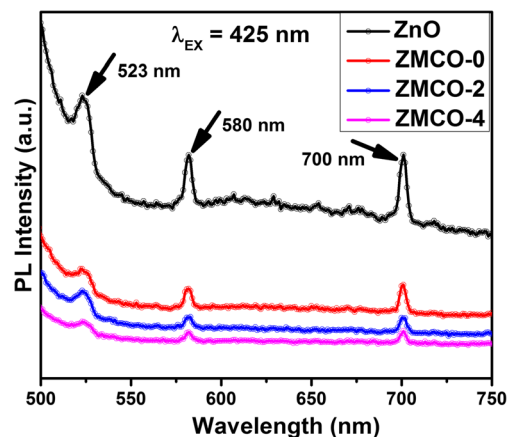
3.6 Photoluminescence Studies

Figure 8 shows the photoluminescence (PL) emission spectra of ZnO, ZMCO-0, ZMCO-2, and ZMCO-4 samples recorded with an excitation wavelength of 425 nm at room temperature [40]. From the figure, three emission

Table 4 Magnetization parameters information of ZnO- and Cu-doped ZnO: Mn nanoparticles from M-H hysteresis curves

S.No.	Sample	M_S (emu/g)	M_R (emu/g)	H_C (G)
1	ZnO	0.0068	0.005	305.72
2	ZMCO-0	0.030	0.016	124.51
3	ZNCO-2	0.032	0.011	56.85
4	ZMCO-4	0.040	0.019	52.48

peaks were observed at about 520 nm, 580 nm, and 700 nm in the spectral region of 500–750 nm. In this figure, it was observed in the ZMCO-0, ZMCO-2, and ZMCO-4 samples that the emission intensity thereof gradually decreased as compared with the ZnO sample and the position of the emission peak slightly shifted towards the higher wavelength side. These results are in accordance with structural, functional, and UV–Vis absorbance study. The recombination of electron–hole pairs corresponds to the transition of electrons from the energy level of the Zn according to the gap state to the valence band state. Generally, in ZnO-based nanomaterials, defects exist with oxygen (V_O) vacancies and zinc (V_{Zn}) vacancies,

Fig. 8 Photoluminescence spectra of ZnO- and Cu-doped ZnO: Mn nanoparticles

depending on various transitions between the valence band and the conduction band. Due to the broad emission of V_O, the V_{Zn}-related defects in the green region are in the range of 511–600 nm but appear in the region having the largest wavelength. In 650–750 nm, more O_i and O_{Zn} correspond to the orange-red region [26, 40]. If the donor defect is a region of major defects in ZnO or Cu-/Mn-doped ZnO, more electrons can be released, improving the generation of oxygen vacancies which enhance the photoactivity, photo current, and magnetization properties in doped samples of ZMCO-0, ZMCO-2, and ZMCO-4.

4 Conclusions

In summary, ZnO, ZMCO-0, ZMCO-2, and ZMCO-4 samples were successfully synthesized by solution combustion method, and their structural, optical, and magnetization properties were investigated. The Mn or Cu/Mn doping samples exhibited Wurtzite structure, and crystallite size is decreased compared to ZnO (36–18 nm). From morphology analysis, all the samples were spherical in shape with porous structure. Compositional analysis spectra confirm that all the selective elements were presented in near stoichiometric ratio. From functional analysis, all bonds were attributed to synthesized samples. From optical absorbance studies, absorption edge shifts towards right side of wavelength denote the decreasing of band gap, and its value varies from 3.32 to 3.04 eV. From magnetization studies, saturation magnetization increases with increase of doping concentration in Cu-/Mn-doped ZnO samples compared to ZnO sample. In photoluminescence studies, the rate of recombination of electron–hole pair process gradually decreased in doped samples compared to ZnO sample. ZMCO-4 shows that the significant enhancement in magnetization may find applications in spintronics and optoelectronic devices. Hence, the systematic investigation on Cu/Mn doping influence on the properties of ZnO may contribute to the progress of the spintronics material research.

References

1. Timm, C.: J. Phys. Condens. Matter. **15**, R1865 (2003)
2. Dobrowolski, W., Kossut, J., Story, T.: Handb. Magn. Mater. **15**, 289 (2003)
3. Kyrychenko, F.V., Ullrich, C.A.: J. Phys. Condens. Matter. **21**, 084202 (2009)
4. Madan, H.R., Sharma, S.C., Suresh, D., Vidya, Y.S., Nagabhushana, H., Rajanaik, H., Anantharaju, K.S., Prashantha, S.C., Maiya, P.S.: Spectrochim. Acta A Mol. Biomol. Spectrosc. **152**, 404 (2016)
5. Silambarasu, A., Manikandan, A., Balakrishnan, K.: J. Supercond. Nov. Magn. **30**, 2631 (2017)
6. Asiri, S., Sertkol, M., Guner, S., Gungunes, H., Batoo, K.M., Saleh, T.A., Sozeri, H., Almessiere, M.A., Manikandan, A., Baykal, A.: Ceram. Int. **44**, 5751 (2018)
7. Valan, M.F., Manikandan, A.: S A Antony. J. Nanosci. Nanotechnol. **15**, 4580 (2015)
8. Meenatchi, B., Deve, K.R.N., Manikandan, A., Renuga, V., Sathiyalakshmi, V.: Adv. Sci. Eng. Med. **8**, 653 (2016)
9. Sumithra, V., Manikandan, A., Durka, M., Jaganathan, S.K., Dinesh, A., Ramalakshmi, N., Antony, S.A.: Adv. Sci. Eng. Med. **9**, 483 (2017)
10. Maruthamani, D., Vadivel, S., Kumaravel, M., Saravanakumar, B., Paul, B.: S S Dhar, A Habibi-Yangjeh, A Manikandan, G Ramadoss. J. Colloid Interface Sci. **498**, 449 (2017)
11. Ravichandran, A.T., Srinivas, J., Karthick, R., Manikandan, A., Baykal, A.: Ceram. Int. **44**, 13247 (2018)
12. Bomila, R., Srinivasan, S., Gunasekaran, S., Manikandan, A.: J. Supercond. Nov. Magn. **31**, 855 (2018)
13. Manikandan, A., Manikandan, E., Meenatchi, B., Vadivel, S., Jaganathan, S.K., Ladchumananandasivam, R., Henini, M., Maaza, M., Aanand, J.S.: J. Alloys Compd. **723**, 1155 (2017)
14. Manikandan, A., Vijaya, J.J., Narayanan, S., Kennedy, L.J.: J. Nanosci. Nanotechnol. **14**, 2507 (2014)
15. Reena, K., Gunaseelan, R., Manikandan, A., Antony, S.A.: Adv. Sci. Eng. Med. **8**, 245 (2016)
16. Amirthavalli, C., Manikandan, A.: AA Prince. Ceram. Int. **44**, 15290 (2018)
17. Babitha, N., Priya, L.S., Christy, S.R., Manikandan, A., Dinesh, A., Durka, M., Arunadevi, S.: J. Nanosci. Nanotechnol. **19**, 2888 (2019)
18. Manikandan, A., Sridhar, R., Antony, S.A., Ramakrishna, S.: J. Mol. Struct. **1076**, 188 (2014)
19. Velanganni, S., Manikandan, A., Prince, J.J., Mohan, C.N., Thiruneelakandan, R.: Phys. B Condens. Matter. **545**, 383 (2018)
20. Chinnaraj, K., Manikandan, A., Ramu, P., Antony, S.A., Neeraja, P.: J. Supercond. Nov. Magn. **28**, 179 (2015)
21. Manikandan, A., Selvam, N., Kennedy, L.J., Kumar, R.T., Vijaya, J.J.: J. Nanosci. Nanotechnol. **13**, 2595 (2013)
22. Manikandan, A., Durka, M., Seevakan, K., Antony, S.A.: J. Supercond. Nov. Magn. **28**, 1405 (2015)
23. Dinesha, M.L., Jayanna, H.S., Mohanty, S., Ravi, S.: J. Alloys Compd. **490**, 618 (2010)
24. Muniraja, P., Kumar, K.S., Ramanadha, M., Sudharani, A., Ravi, M., Vijayalakshmi, R.P.: J. Supercond. Nov. Magn. **32**, 2175 (2019)
25. Eppakayala, J., Mettu M. R., Pendyala, V. R., Madireddy, J. R.: Mater. Today: Proc. (2019) https://doi.org/10.1016/j.matpr.2019.08.099
26. Godavarti, U., Mote, V.D., Reddy, M.R., Nagaraju, P., Kumar, Y.V., Dasari, D.T., Dasari, M.P.: Phys. B Condens. Matter. **553**, 151 (2019)
27. Irshad, K., Khan, M.T., Murtaza, A.: Phys. B Condens. Matter. **543**, 1 (2018)
28. Kalita, A., Kalita, M.P.: Phys. B Condens. Matter. **552**, 30 (2019)
29. Othman, A.A., Osman, M.A., Ibrahim, E.M., Ali, M.A., Abd-Elrahim, A.G.: Mater. Sci. Eng. B **219**, 1 (2017)
30. Sahai, A., Goswami, N.: Phys. E: Low-Dimension. Syst. Nanostruct. **58**, 130 (2014)
31. Ansari, S.A., Nisar, A., Fatma, B., Khan, W., Naqvi, A.H.: Mater. Sci. Eng. B **177**, 428 (2012)
32. Zak, A.K., Abrishami, M.E., Majid, W.A., Yousefi, R., Hosseini, S.M.: Ceram. Int. **37**, 393 (2011)
33. Xiong, G., Pal, U., Serrano, J.G., Ucer, K.B., Williams, R.T.: Phys. Status Solidi C. **3**, 3577 (2006)
34. Dolgonos, A., Mason, T.O., Poeppelmeier, K.R.: J. Solid State Chem. **240**, 43 (2016)
35. Kamarulzaman, N., Kasim, M.F., Rusdi, R.: Nanoscale Res. Lett. **10**, 346 (2015)

36. Kamarulzaman, N., Kasim, M.F., Chayed, N.F.: Results Phys. **6**, 217 (2016)

37. Singh, N.S., Singh, S.D., Bandyopadhyay, S.K.: Phys. Procedia. **54**, 2 (2014)

38. Zou, Y., Qu, Z., Fang, J., Zhang, Y.: J. Magn. Magn. Mater. **321**, 3352 (2009)

39. Pal, B., Giri, P.K.: J. Appl. Phys. **108**, 084322 (2010)

40. Gao, D., Zhang, Z., Fu, J., Xu, Y., Qi, J., Xue, D.: J. Appl. Phys. **105**, 113928 (2009)